16th World Conference on Earthquake Engineering, 16WCEE 2017

Santiago Chile, January 9th to 13th 2017

Paper N° 950

Registration Code: S- A1463087629

ESTIMATING FAULT DISTANCES WITHOUT A FAULT

E. M. Thompson[(1)], C. B. Worden[(2)]

(1) U.S. Geological Survey, Golden, Colorado, emthompson@usgs.gov
(2) Synergetics, Inc., 1520 South College Ave., Fort Collins, Colorado 80524, cbworden@usgs.gov

Abstract

Most ground motion prediction equations (GMPEs) require finite-fault distance metrics, such as the distance to the surface projection of the rupture (R_{JB}) or the closest distance to the rupture plane (R_{RUP}). There are a number of situations in which GMPEs are used where it is either necessary or advantageous to compute the finite-fault distances from point-source distances, such as hypocentral (R_{HYP}) or epicentral distances (R_{EPI}). For ShakeMap [1], it is necessary to provide an estimate of the shaking levels for events without finite fault models, and before finite faults are available for events that eventually do have finite fault models. In probabilistic seismic hazard analysis (PSHA), it is often convenient to use point-source distances for gridded seismicity sources, particularly if a preferred orientation is unknown. This avoids the computationally cumbersome task of computing fault-based distances for virtual faults across all strikes for each source. As recommended by Bommer and Akkar [2], it would be ideal if GMPE developers provided coefficients for point-source distances as an alternative to fault-based distances (as done by Akkar et al. [3]), but these are rarely available. In the 2008 version of the U.S. national seismic hazard model [4], equations were derived for the average finite fault distance as a function of R_{EPI} for vertical faults as a function of earthquake magnitude. Here, we follow the same method but extend it to allow for dipping faults. Since the dip is also not known in many cases, we provide correction factors that assume an average dip associated with each mechanism. Additionally, we derive adjustment factors for the inter- and intra-event standard deviations of GMPEs that reflect the added uncertainty in the ground motion estimation when point-source distances are used to estimate the finite-fault distances.

Keywords: Extended, finite, point, distance, conversion, rupture, epicenter

1. Introduction

In ground motion prediction equations (GMPEs), the decay of the ground motion intensity measure (e.g., peak ground motion, response spectra) with distance is most commonly taken into account with definitions of distance from the ruptured area (i.e., the portion of the fault where coseismic slip exceeds some threshold). In this article, we refer to this class of distance measures as finite-fault distances, and two of the most commonly used examples are the Joyner-Boore distance (the horizontal distance to the surface projection of the rupture [5]; R_{JB}) and the rupture distance (the closest distance to the rupture; R_{RUP}). A finite fault model often does not exist, however, and the only available distances are point-source distances, such as hypocentral (R_{HYP}) or epicentral distance (R_{EPI}). There are a number of situations in which GMPEs are used where it is either necessary or advantageous to estimate the finite-fault distances from a point-source distance. For ShakeMap, it is necessary to provide an estimate of the shaking levels before a finite fault is available, although this is updated when (and if) a finite fault model becomes available. In a probabilistic seismic hazard analysis (PSHA), it is often convenient to use point-source distances for gridded seismicity, particularly if a preferred rupture orientation is unknown, as is done in the U.S. Geological Survey (USGS) National Seismic Hazard Models (NSHMs) [4]. This approach avoids the computationally cumbersome task of computing fault-based distances for virtual faults across all possible strikes and dips for each source. Monelli et al. [6] performed PSHA sensitivity tests and showed that the difference between the use of finite fault distances vs point-source distances can result in differences in the design ground motions by as much as 58%.

Ideally, as recommended by Bommer and Akkar [2], GMPE developers would provide a separate set of regression coefficients for the use of point-source distances as an alternative to fault-based distances (as done by Akkar et al. [3]), but such models are rarely available. An alternative is to convert point-source distances to median fault-based distances using equations such as those developed in the Electric Power Research Institute (EPRI) report on ground motion models for the central and eastern United States (CEUS) [7]. These equations were based on ground motion simulations for vertical strike-slip faults and dipping reverse faults (where the dip angle is fixed at 40°). The EPRI approach determined point-source distance adjustments that produced the median (simulated) ground motions from a specific set of GMPE functional forms. The report provides equations for adjusting the uncertainty of the GMPE predictions to account for the additional uncertainty of the unknown fault distance. Around the same time, Scherbaum et al. [8] developed a methodology to convert from point-source distances to finite-fault distances using simulations of rupture and observational statistics from which parametric models of distance residuals were derived. Chiou and Youngs [9] (Appendix B) followed a similar approach to fill in the finite fault distances for events without finite fault models in their analysis.

The USGS NSHMs (see Petersen et al. [4]; Appendix C) use conversion factors based on numerical integration of a vertical fault rotated through non-redundant strike angles, where the length of the rupture is computed from the earthquake magnitude using the empirical relationships between magnitude and rupture length developed by Wells and Coppersmith [10] (hereafter termed WC94) equations. However, the NSHMs do not propagate the additional uncertainty introduced by the unknown rupture geometry. Bommer et al. [11] developed distance conversion equations by randomly sampling epicenter/receiver locations and fault rupture lengths, also assuming a vertical fault and the WC94 magnitude-length relationships.

In this article, we develop conversion equations that extend the above methodologies. Rather than randomizing or simulating fault and site parameters, we numerically integrate the conversion factors in a manner similar to the method described in Appendix C of Petersen et al. [4]. However, we extend the integration to account for variability in dip, mechanism, and rupture area. The result is a set of generic distance and uncertainty conversion factors that can be applied to existing GMPEs under various circumstances. We develop a series of distance conversion relationships (and the resulting additional uncertainty in the estimation of the finite-fault distances) for common situations, but we also provide software [12] where the assumptions can be specified for new situations. We then demonstrate how to incorporate these equations into a GMPE.

2. Seismological Constraints

The relationship between point-source and finite-fault distances depends on a number of factors, such as dip, rupture area and aspect ratio, and the depth range of the seismogenic zone. In this section, we describe the assumptions that we have made to constrain these parameters. Since these parameters are often unknown, we represent them with probability distributions. The assumptions are summarized in Table 1 and described in more detail below.

Table 1 – Distance conversion assumptions for various scenarios.

Description	M-A Reference	Mechanism	Aspect ratio	Seis. range (km)	Dip (km)
Default	[10]	All	1.7	0-20	U(0, 90)
ACR N	[10]	N	1.7	0-20	U(40, 60)
ACR R	[10]	R	1.7	0-20	U(35, 50)
ACR SS	[10]	SS	1.7	0-20	U(75, 90)
SCR N	[13]	N	1.0	0-15	U(40, 60)
SCR R	[13]	R	1.0	0-15	U(30, 60)
SCR SS	[13]	SS	1.0	0-15	U(60, 90)

M-A: magnitude-area relationship.
Seis. Range: Seismogenic zone depth range.
U(a, b): Uniformly distributed from a to b.
ACR; SCR: Active crustal region; stable continental region
N, R, SS: Normal, reverse, strike slip faulting.

For rupture area, we use magnitude-area relationships. These relationships are based on linear regression of the logarithm of the rupture area with magnitude. Thus, for a given magnitude, the mean and standard deviation of the logarithm of the rupture area have been computed. However, the magnitude area relationship varies between tectonic environments. For active crustal regions (ACRs) we use the WC94 equations; for stable continental regions (SCRs) we use the equation developed by Somerville [13]. The WC94 equations vary by mechanism, and provide an 'all' category for when the mechanism is unknown; in contrast, Somerville [13] does not provide different coefficients for different mechanisms. If the mechanism is known, we also use it to constrain the probability distribution of dip. For an unknown mechanism, we assume the dip is uniformly distributed between zero and 90 degrees. Note that a larger minimum value for dip might be more reasonable for this general case. Adjustments like this can easily be accommodated since the source code for these calculations is freely available. For ACRs, we inspected the range of dip angles by mechanism in the NGA-W2 database [14, 15] and selected approximate representative ranges, as summarized in Table 1. For SCRs, we used the range in dips for each mechanism reported in the CEUS-SSC report [16]. Similarly, we base the seismogenic zone depth range for SCRs on the CEUS-SSC report [16]. For ACRs, we set the seismogenic zone depth range to 0-20 km based on the hypocentral depth range seen in the NGA-W2 database [15]. Note that we also should assume a probability distribution for the aspect ratio (AR) (i.e., the ratio of rupture length to rupture width). However, for simplicity, we assume a fixed value for AR. For ACRs, we used an AR of 1.7, which is the average aspect ratio in the NGA-W2 database for events with magnitude less than 6.7. This threshold magnitude was selected to avoid events that are width-limited by the seismogenic zone. For SCRs, following the CEUS-SSC report [16] we used an AR of 1.0. In both cases, the AR is adjusted as a function of rupture area and dip angle to ensure that the seismogenic zone depth range is not violated. If the reader finds these choices unsatisfactory for specific applications, we provide the software that we use for our calculation [12], which allows the selection of other assumptions and could easily be modified to include a probability distribution for AR.

3. Joyner-Boore Distance

In Appendix C of Petersen et al. [4], S. Harmsen derived equations for the mean R_{JB} ($\bar{R}_{JB}$) of a vertical fault as a function of epicentral distance (R_{EPI}) and earthquake magnitude (**M**), using the WC94 empirical relationship between rupture length (L) and **M**. Although written in a different form/notation, Harmsen essentially solved the following integral

$$\bar{R}_{JB}(R_{EPI}, \mathbf{M}) = \int_0^{2\pi} R_{JB}(R_{EPI}, \theta) P(\theta) d\theta \tag{1}$$

where θ is the angle between the vector from epicenter (E) to site (S) and the normal to the fault strike. Here, we follow the same method but extend it to allow for dipping faults, position of the hypocenter (H) on the rupture plane, and uncertainty in the fault dimensions. Since we allow the faults to dip, we need to also compute the fault width (W). Thus, rather than using the WC94 equations for $L = f(\mathbf{M})$, we use their equations for computing the rupture area (A) from **M** and then compute L and W from A and AR. Harmsen assumed that H is located in the center of the fault (allowing for simplification due to the symmetry of the problem); however, we assume that the along-strike distance (y) and along-width distance (x) are uniformly distributed. Fig. 1 illustrates the geometry of our formulation.

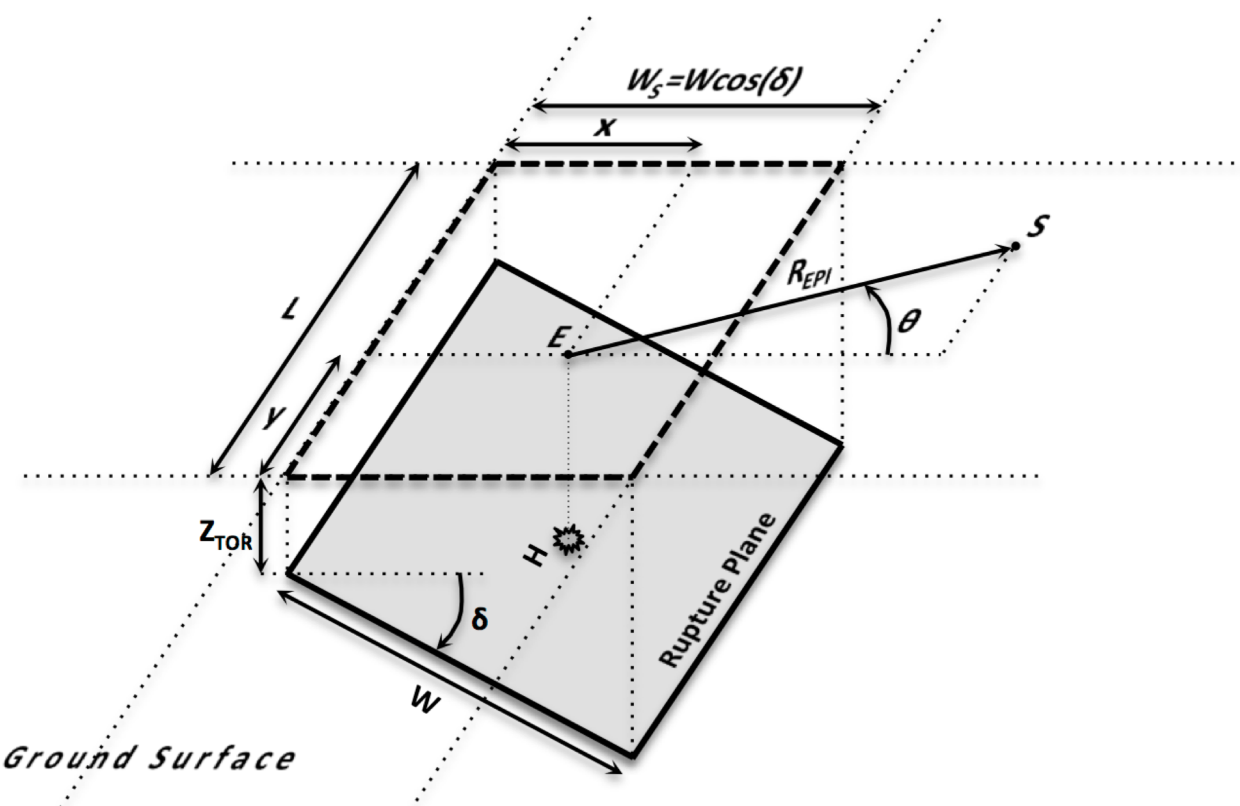

Fig. 1 – Schematic illustration of epicenter-to-site geometry. The heavy dashed line represents the surface projection of the rupture plane. The rupture plane has (along-strike) length L, (down-dip) width W, and dip δ.

Our generalization for the average R_{JB} for an unknown strike and location of the hypocenter on the fault plane is

$$\bar{R}_{\mathrm{JB}}(R_{\mathrm{EPI}},\mathbf{M}) = \int_{-\infty}^{\infty}\int_{0}^{\pi/2}\int_{0}^{L}\int_{0}^{W_S}\int_{0}^{2\pi} R_{\mathrm{JB}}(R_{\mathrm{EPI}},\mathbf{M},\theta,x,y,\delta,\epsilon) \times P(\theta)P(x)P(y)P(\delta)P(\epsilon)\, d\theta\, dx\, dy\, d\delta\, d\epsilon \quad (2)$$

where $W_S = W\cos(\delta)$ is the width of the surface projection of the fault, δ is fault dip, and ϵ is the quantile of $\log(A)$, which is assumed to be normally distributed with mean and standard deviations computed from $\mathbf{M}$. To evaluate equation 2, we must also make assumptions about the probability distributions of θ (uniform from zero to 2π), x (uniform from zero and W_S), y (uniform from zero and L), δ (uniform from zero to $\pi/2$), and a truncation level for ϵ (±3 standard deviations). We evaluate equation 2 with the trapezoidal method of numerical integration. The probability distributions of the different variables can be adjusted for different conditions (e.g., focal mechanism, tectonic environment) or even be set to constant values for a specific event or for illustrative

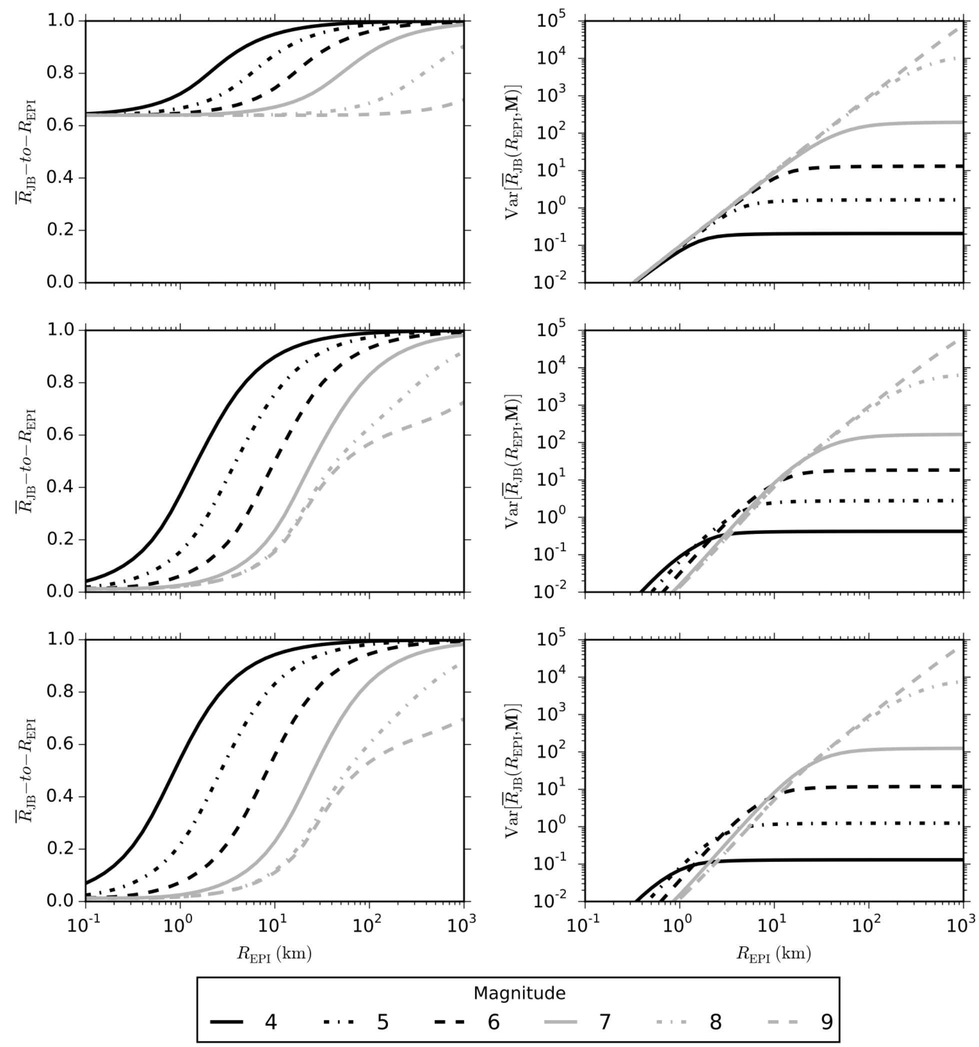

Fig. 2 – $\bar{R}_{\mathrm{JB}}$-to-R_{EPI} ratio (left) and $\mathrm{Var}[\bar{R}_{\mathrm{JB}}(R_{\mathrm{EPI}},\mathbf{M})]$ (right) curves for strike-slip (top), normal (middle), and reverse mechanisms (bottom), assuming average dips of 90°, 50°, and 40°, respectively.

purposes.

Following Kaklamanos et al. [17], we assume constant dips of 90°, 50°, and 40°, for strike slip, normal, and reverse mechanisms, respectively. Fig. 2 gives the ratio of $\bar{R}_{\mathrm{JB}}$-to-R_{EPI} for each mechanism for **M** 4 to **M** 9. These curves use the default assumptions listed in Table 1, except that the dip angle is fixed at a constant value for this illustration. The curves for strike-slip are roughly equivalent to those by Harmsen (in [4]). The ratio does not approach zero at small R_{EPI} because the surface projection of the fault has zero width for vertical faults, and so $P(R_{\mathrm{JB}}=0)=0$. The differences between the curves for the different mechanisms are largely determined by the assumed mean dips; as the dip decreases, the width of the surface projection of the fault increases, decreasing R_{JB}.

Generally, we cannot constrain δ as in Fig. 2. In the absence of additional information about the earthquake, we compute $\bar{R}_{\mathrm{JB}}$ and its variance [$\mathrm{Var}(\bar{R}_{\mathrm{JB}})$] with the default assumptions in Table 1 (we omit the equations for the $\mathrm{Var}[\bar{R}_{\mathrm{JB}}(R_{\mathrm{EPI}},\mathbf{M})]$ since they are just a small variation on the equation for the mean). However, we generally know the tectonic environment and focal mechanism, which allows us to constrain some of these parameters further, as summarized in Table 1. We plot the $\bar{R}_{\mathrm{JB}}$-to-R_{EPI} ratio and $\mathrm{Var}[\bar{R}_{\mathrm{JB}}(R_{\mathrm{EPI}},\mathbf{M})]$ curves in Fig. 3 for three different sets of assumptions in Table 1. The three examples are for the default assumptions, for a strike-slip mechanism in active crustal regions (ACR), and for a strike-slip mechanism in stable continental

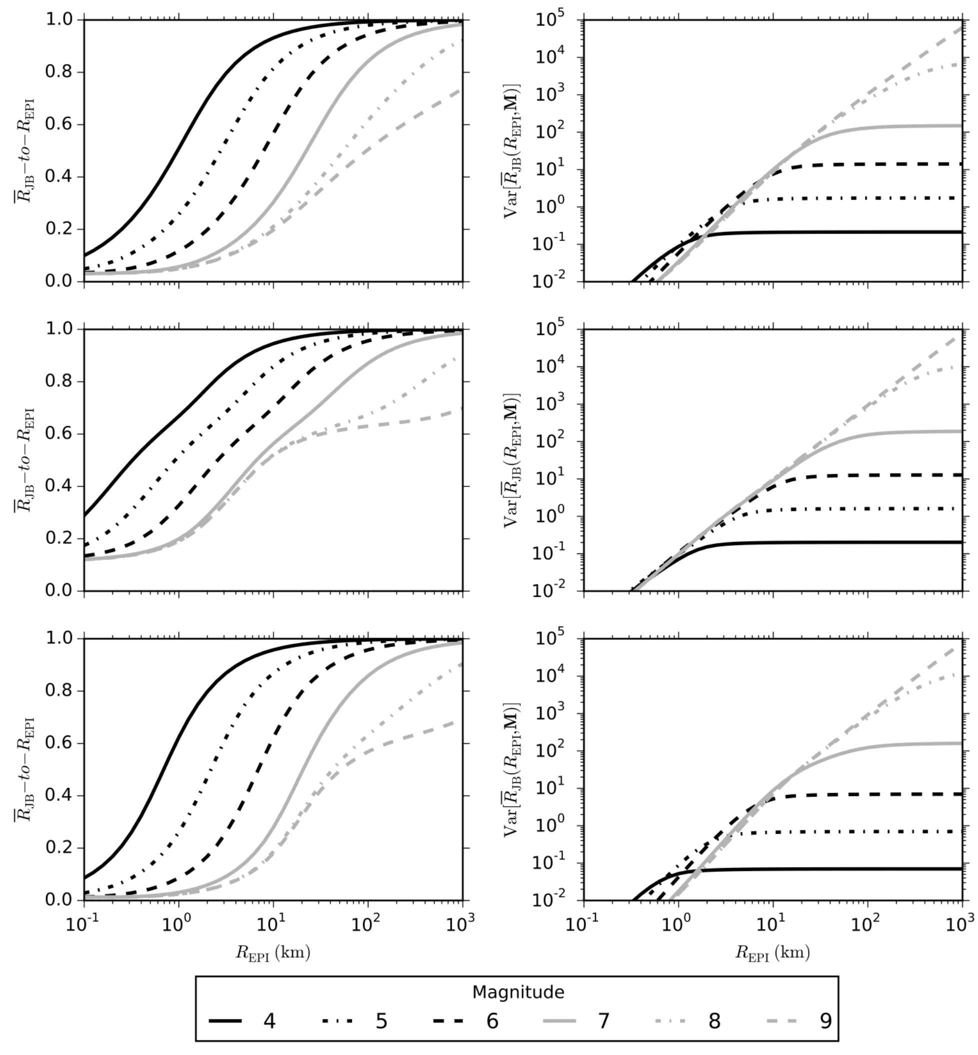

Fig. 3 – $\bar{R}_{\mathrm{JB}}$-to-R_{EPI} ratio (left) and $\mathrm{Var}[\bar{R}_{\mathrm{JB}}(R_{\mathrm{EPI}},\mathbf{M})]$ (right) curves for the default assumptions in Table 1 (top), an ACR strike slip event (middle), and SCR reverse event (bottom).

regions (SCR); the mechanisms were selected to be the most common mechanism in the respective tectonic environments.

4. Rupture Distance

In order to compute R_{RUP}, the depth to the top of the rupture (Z_{TOR}) is also required. Thus, we must add an integral across possible values of Z_{TOR} to equation 2 as follows:

$$\bar{R}_{\mathrm{RUP}}(R_{\mathrm{EPI}},\mathbf{M}) = \int_0^z \int_{-\infty}^{\infty} \int_0^{\pi/2} \int_0^L \int_0^{W_S} \int_0^{2\pi} R_{\mathrm{RUP}}(R_{\mathrm{EPI}},\mathbf{M},\theta,x,y,\delta,\epsilon,Z_{\mathrm{TOR}}) \times P(\theta)P(x)P(y)P(\delta)P(\epsilon)P(Z_{\mathrm{TOR}})\, d\theta\, dx\, dy\, d\delta\, d\epsilon\, dZ_{\mathrm{TOR}} \tag{3}$$

where Z_{TOR} is assumed to be uniformly distributed between zero and z, and z is constrained by fault width, dip, and the seismogenic zone depth range at each integration step. Fig. 4 plots the same information for the same set of assumptions as Fig. 3; note that unlike the $\bar{R}_{\mathrm{JB}}$-to-R_{EPI} ratio, the $\bar{R}_{\mathrm{RUP}}$-to-R_{EPI} is greater than 1 for small values of R_{EPI}; this aspect of the curves is controlled by the distribution of Z_{TOR}. Since z will be smaller for

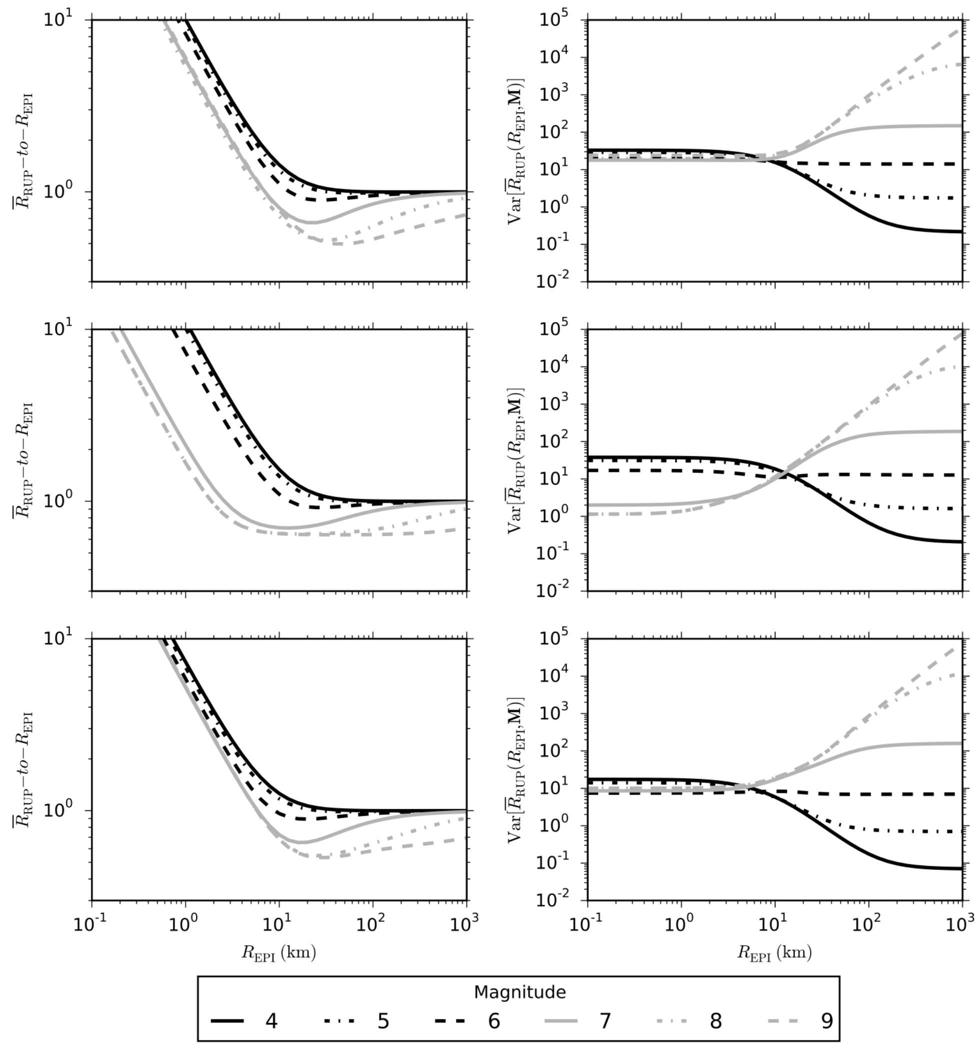

Fig. 4 – $\bar{R}_{\mathrm{RUP}}$-to-R_{EPI} ratio (left) and $\mathrm{Var}[\bar{R}_{\mathrm{RUP}}(R_{\mathrm{EPI}},\mathbf{M})]$ (right) curves for the default assumptions in Table 1 (top), an ACR strike slip event (middle), and SCR reverse event (bottom).

larger faults, at small values of R_{EPI} the maximum value of $\bar{R}_{\mathrm{RUP}}$ tends to be smaller for larger magnitudes.

5. GMPE Standard Deviations

Using $\bar{R}$ (meaning $\bar{R}_{\mathrm{JB}}$ or $\bar{R}_{\mathrm{RUP}}$) in place of R (meaning R_{JB} or R_{RUP}) in a GMPE increases the uncertainty of the output. To account for this, we adjust the GMPE standard deviation using standard error propagation techniques [18] to be

$$\sigma_T = \sqrt{\sigma_G^2 + \Delta\sigma^2}\,, \tag{4}$$

and

$$\Delta\sigma^2 = \left(\frac{\partial(\ln Y)}{\partial R}\right)^2 \mathrm{Var}[\bar{R}(\mathbf{M})]\,, \tag{5}$$

where $\ln Y$ is the natural logarithm of the response spectra predicted by the GMPE, and σ_G is its total standard deviation predicted by the GMPE. In most cases, it will only be practical to compute the derivative of the GMPE in equation 5 numerically. But for this paper, we use the Boore et al. [19] GMPE, and its derivative with respect to R_{JB} can be found analytically to be

$$\frac{\partial\,(\ln Y)}{\partial R_{JB}} = \frac{\partial F_P}{\partial R_{JB}} \cdot \left(1 + \frac{f_2\,\cdot\,PGA_r}{f_3 +\,PGA_r}\right), \tag{6}$$

where

$$\frac{\partial F_P}{\partial R_{JB}} = \,R_{JB}\left\{\frac{1}{R^2}\left[c_1 + c_2\left(M - M_{ref}\right)\right] + \frac{1}{R}(c_3 + \Delta c_3)\right\}, \tag{7}$$

and PGA_r (the PGA predicted for rock) is derived from equation 1 of Boore et al. [19] using a V_{S30} of 760 m/s. The constants $c_1, c_2, c_3, \Delta c_3$, and f_3 are given by Boore et al. [19] for the ground motion measure in question. R and f_2 are given by Boore et al. [19] equations 4 and 8, respectively. Fig. 5 shows the $\Delta\sigma$ that we compute from equation 5 with the Boore et al. [19] GMPE and compares it to the analogous EPRI [7] equations. The EPRI

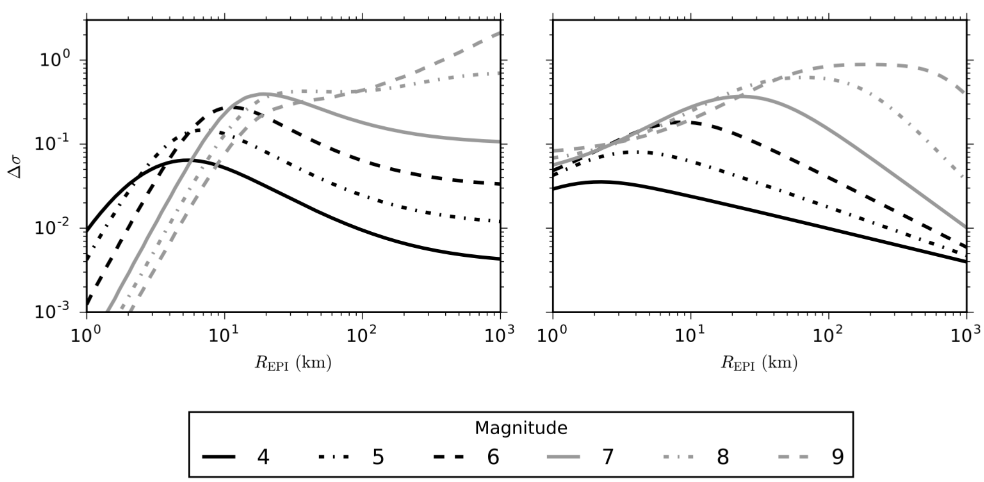

Fig. 5 – $\Delta\sigma$ computed from equation 5 using the Boore et al. [19] GMPE (left), and the analogous equations by EPRI [7] (right).

report provides different coefficients for different GMPE functional forms and for different oscillator periods. In Fig. 5, we used the coefficients for their F1 functional form and PGA. Note that our results are in general agreement in terms of the magnitude of the $\Delta\sigma$ term; the minor differences result from different assumptions of the distribution of source parameters (e.g., dip) and in how the misfit function was defined in optimizing the distance adjustment factors (our factors are not dependent on a GMPE functional form).

6. Evaluation and Interpolation

We explored the possibility of approximating the ratio and variance curves such as those in Figs. 3 and 4 with simple parametric functions. However, the irregular shape of the curves makes it difficult to achieve an accurate approximation with few parameters. So rather than parametrically approximating the ratios, variances, and/or delta sigma values (which are GMPE-specific) we decided to retain as much precision as possible and tabulate these values directly. For each row in Table 1, we provide four tables: two for R_{JB} and two for R_{RUP}; for each of the distances, we provide a table of the mean finite fault distance to R_{EPI} ratio and a table for the respective variances. The tables are arranged with rows for values of R_{EPI} logarithmically spaced from 0.1 to 1000 km and the columns are for magnitudes from **M** 4 to 9 incremented by 0.25 magnitude units. An abridged example table is given in Table 2.

Table 2 – Abridged example of tabulated values of $\bar{R}_{\mathrm{JB}}$-to-R_{EPI} ratios.

$\boldsymbol{R_{\mathrm{EPI}}}$ **(km)**	**M 4**	**M 4.25**	**M 4.5**	**M 4.75**	**M 5**
0.1	0.234821	0.194306	0.161197	0.135113	0.115207
0.125893	0.272624	0.226096	0.187094	0.155453	0.130702
0.158489	0.315243	0.262731	0.217688	0.180158	0.149952
0.199526	0.362271	0.304161	0.253124	0.209575	0.173506
0.251189	0.413028	0.35011	0.293356	0.243813	0.20178
0.316228	0.466496	0.400042	0.338218	0.282854	0.234821
0.398107	0.521417	0.452955	0.387248	0.326583	0.272624
0.501187	0.57673	0.507611	0.439522	0.374658	0.315243
0.630957	0.631557	0.562923	0.493841	0.426204	0.362271
0.794328	0.684747	0.617962	0.549095	0.480128	0.413028
1	0.734804	0.671643	0.604266	0.535253	0.466496
1.258925	0.780243	0.722666	0.658395	0.590512	0.521417
1.584893	0.819936	0.769406	0.710275	0.645034	0.57673
1.995262	0.85361	0.810579	0.758214	0.697632	0.631557
2.511886	0.881639	0.845742	0.800839	0.746672	0.684747
3.162278	0.904683	0.875127	0.837512	0.790721	0.734804
3.981072	0.923472	0.899349	0.868292	0.828912	0.780243
5.011872	0.9387	0.919135	0.893738	0.861123	0.819936
6.309573	0.950986	0.935192	0.914565	0.887838	0.85361
7.943282	0.960864	0.94816	0.931491	0.909751	0.881639
10	0.968786	0.958594	0.945175	0.927588	0.904683

To evaluate the ratios/variances at an arbitrary R_{EPI} and magnitude, we prefer to interpolate distance logarithmically and magnitude linearly. Additionally, we suggest that if one must extrapolate outside of the range in magnitude and distance for the tabulated values, then the nearest tabulated point should be used.

7. Discussion

We have provided point-source distance adjustments to get approximations of finite fault distances for a handful of general tectonic environments. This method can be easily adjusted to allow for different distributions that would be more appropriate for more specific projects/regions. Note that a logical extension of this work is to avoid integrating across all azimuths by building tables of adjustment factors and sigma for a given magnitude, varying the angle between the strike and backazimuth of each site. This allows for better constraints on the orientation of the rupture when strike is known. Also, we have not yet addressed subduction zone earthquakes because we think that additional work is needed. In particular, it will be important to constrain the distributions differently for interface and intraslab events. For large interface events, it is probably important to make use of a model of subduction zone geometry (such as [20]) to derive correction factors that make use of distributions that are conditioned on the orientation of the slab model at the location of the earthquake.

8. Conclusions

We have provided a method for adjusting point source distances to get mean finite fault distances. This is particularly useful for applications like ShakeMap where we frequently must estimate the ground motions before a finite fault model is available. These types of adjustments are also useful for gridded seismicity in probabilistic seismic hazard analysis. Additionally, we were surprised to see significant differences between the mean finite fault distances and the point source distances extend to such small magnitudes. For example, we see that $\bar{R}_{\mathrm{JB}}$ is as much as 20% less than R_{EPI} at distances as large as 30 km for a magnitude 6 earthquake. For this reason, we think that it would also be appropriate for GMPE developers to use this type of adjustment for records that are in their analysis but do not have a finite fault model.

9. Acknowledgements

We thank Peter Powers and Janet Slate for providing valuable comments and edits that improved this paper.

10. References

[1] Worden CB, Wald DJ ShakeMap Manual. *doi:10.5066/F7D21VPQ*.

[2] Bommer JJ, Akkar S (2012): Consistent source-to-site distance metrics in ground-motion prediction equations and seismic source models for PSHA. *Earthq. Spectra*, **28**(1), 1–15.

[3] Akkar S, Sandıkkaya MA, Bommer JJ (2014): Empirical ground-motion models for point- and extended-source crustal earthquake scenarios in Europe and the Middle East. *Bull. Earthq. Eng.*, **12**(1), 359–387.

[4] Petersen MD, Moschetti MP, Powers PM, Mueller CS, Haller KM, Frankel AD, Zeng Y, Rezaeian S, Harmsen SC, Boyd OS (2014): Documentation for the 2014 update of the United States national seismic hazard maps. U.S. Geological Survey. U.S. Geological Survey Open-File Report 2014–1091.

[5] Joyner WB, Boore DM (1981): Peak horizontal acceleration and velocity from strong-motion records including records from the 1979 Imperial Valley, California, earthquake. *Bull. Seismol. Soc. Am.*, **71**(6), 2011–2038.

[6] Monelli D, Pagani M, Weatherill G, Danciu L, Garcia J (2014): Modeling distributed seismicity for probabilistic seismic-hazard analysis: Implementation and insights with the OpenQuake engine. *Bull. Seismol. Soc. Am.*, **104**(4), 1636–1649.

[7] Electric Power Research Institute, Inc. (EPRI) (2003): CEUS Ground Motion Project: Model Development and Results. Palo Alto, CA: Electric Power Research Institute, Inc. (EPRI). 1008910.

[8] Scherbaum F, Schmedes J, Cotton F (2004): On the conversion of source-to-site distance measures for extended earthquake source models. *Bull. Seismol. Soc. Am.*, **94**(3), 1053–1069.

[9] Chiou BSJ, Youngs RR (2008): NGA model for average horizontal component of peak ground motion and response spectra. Pacific Engineering Research Center. PEER Report 2008/09.

[10] Wells DL, Coppersmith KJ (1994): New empirical relationships among magnitude, rupture length, rupture width, rupture area, and surface displacement. *Bull. Seismol. Soc. Am.*, **84**(4), 974–1002.

[11] Bommer JJ, Dost B, Edwards B, Stafford PJ, van Elk J, Doornhof D, Ntinalexis M (2016): Developing an Application-Specific Ground-Motion Model for Induced Seismicity. *Bull. Seismol. Soc. Am.*

[12] Thompson EM, Worden CB (2016): Point-Source Finite-Fault Distance Convers, *doi: 10.5066/F7VH5M0W.*

[13] Somerville PG (2014): Scaling Relations between Seismic Moment and Rupture Area of Earthquakes in Stable Continental Regions. PEER Report 2014/14.

[14] Ancheta TD, Darragh RB, Stewart JP, Seyhan E, Silva WJ, Chiou BS, Wooddell KE, Graves RW, Kottke AR, Boore DM, Kishida T, Donahue, Jennifer L. (2013): PEER NGA-West2 Database. University of California, Berkeley: Pacific Earthquake Engineering Research Center. PEER Report 2013/03.

[15] Ancheta TD, Darragh RB, Stewart JP, Seyhan E, Silva WJ, Chiou BS-J, Wooddell KE, Graves RW, Kottke AR, Boore DM (2014): NGA-West2 database. *Earthq. Spectra*, **30**(3), 989–1005.

[16] Electric Power Research Institute, Inc. (EPRI) (2012): Central and Eastern United States seismic source characterization for nuclear facilities. Palo Alto, California: EPRI, U.S. DOE, and U.S. NRC.

[17] Kaklamanos J, Baise LG, Boore DM (2011): Estimating unknown input parameters when implementing the NGA ground-motion prediction equations in engineering practice. *Earthq. Spectra*, **27**(4), 1219–1235.

[18] Ku HH (1966): Notes on the use of propagation of error formulas. *J. Res. Natl. Bur. Stand.*, **70**(4).

[19] Boore DM, Stewart JP, Seyhan E, Atkinson GM (2014): NGA-West2 equations for predicting PGA, PGV, and 5% damped PSA for shallow crustal earthquakes. *Earthq. Spectra*, **30**(3), 1057–1085.

[20] Hayes GP, Wald DJ, Johnson RL (2012): Slab1.0: A three-dimensional model of global subduction zone geometries. *J. Geophys. Res. Solid Earth*, **117**(B1).